Applied Catalysis B: Environmental 201 (2017) 543–551

Contents lists available at ScienceDirect

Applied Catalysis B: Environmental

journal homepage: www.elsevier.com/locate/apcatb

Mesoporous manganese oxides for NO_2 assisted catalytic soot oxidation

Niluka D. Wasalathanthri[a], Thomas M. SantaMaria[a], David A. Kriz[a], Shanka L. Dissanayake[a], Chung-Hao Kuo[a], Sourav Biswas[a], Steven L. Suib[a,b,*]

[a] Department of Chemistry, University of Connecticut, U-3060, 55 North Eagleville Road, Storrs, CT 06269, United States
[b] Institute of Materials Science, University of Connecticut, U-3060, 55 North Eagleville Road, Storrs, CT 06269, United States

ARTICLE INFO

Article history:
Received 31 May 2016
Received in revised form 13 August 2016
Accepted 22 August 2016
Available online 23 August 2016

Keywords:
Soot
NO_2
Mesoporous
Manganese oxide
Oxygen spill-over

ABSTRACT

Air pollution issues due to soot/diesel particulate matter (DPM) emitted from incomplete burning of diesel fuel have become a global issue in this century. A series of manganese oxides, namely amorphous manganese oxide (Meso-Mn-A), Mn_2O_3 (Meso-Mn_2O_3), MnO_2 (epsilon phase) (Meso-ε-MnO_2) and octahedral molecular sieves MnO_2 (Meso-OMS-2) was synthesized via a soft template method. The potential of mesoporous manganese oxides in acceleration of NO_2 assisted catalytic oxidation of diesel soot (Printex-U) under lean conditions was investigated. The physiochemical properties of synthesized materials were systematically characterized by X-ray diffraction, N_2-sorption, high-resolution transmission electron microscopy, and H_2-temperature programmed reduction. A series of temperature programmed oxidation experiments was carried out to investigate the effect of feed gas composition on activity of the catalyst, and TGA-MS experiments were done to calculate the kinetic energy for each system. Mesoporous manganese oxides were found to be effective for complete oxidation of diesel soot under exhaust gas temperatures, and activities of all the manganese oxides were increased in the presence of NO_2 in the feed gas. Meso-ε-MnO_2 possesses the highest performance, exhibiting the lowest T_i and T_m (230 °C and 305 °C), the narrowest temperature range (75 °C), and the lowest E_a (298 kJ mol^{-1}). The ability to oxidize soot in the presence of NO_2 makes these materials economical and ecofriendly catalysts for use in continuous regeneration traps.

1. Introduction

Diesel engines are considered to be the most effective combustion motors, and hence are used for a broad range of technical applications, such as automobiles, locomotives, ships, and power generators [1,2,3]. Despite the high efficiency of diesel engines, diesel particulate matter (DPM) or simply soot is an unsolicited byproduct emitted by diesel exhaust engines. Soot can not only foul the exhaust system, but also cause severe respiratory hazards such as asthma, bronchitis, and lung cancers when inhaled [1–8]. Consequently, emission threshold limits have been established and constantly tightened due to the increased emission of DPM over the last two decades [2,9]. The use of diesel particulate filters (DPFs) to trap DPM is a general post treatment technology to meet the stringent emission standards [6]. However, the DPFs require periodic regeneration, otherwise the backpressure created by the loaded DPF may potentially decrease the efficiency of the engine [1,2,4,6,10–12]. The most popular regeneration technique is using a continuous regeneration trap, in which platinum containing catalysts are located upstream in the filter which oxidize the NO emitted by the engine to NO_2. The generated NO_2 is a better oxidant than O_2, and is potentially useful to oxidize DPM at exhaust gas temperatures (200–500 °C) [1,2,9,11,13]. In this context, it is very important to identify a promising catalyst which is active for NO_2 assisted soot combustion at exhaust gas temperatures. Numerous catalytic materials such as precious metal containing catalysts (i.e., Pt, Ag, Au) [1,5,8,9,14–16], spinels (i.e., $ZnAl_2O_4$, $CuFe_2O_4$,) [17,18], perovskites (i.e., $SrTiO_3$, $MgTiO_3$) [17], transition metal oxides (i.e., Mn, Cu, Co, Ti, Zr, Ce) [2,19–21], mixed metal oxides (i.e., MnO_x—CeO_2, CoO_x—CeO_2, CuO—CeO_2, $Ce_{0.5}Pr_{0.5}O_2$) [3,10,11,13,22–24], have been studied over the years.

The key factor that determines the activity of catalytic soot oxidation is the transfer of oxygen from its surface to the soot [2,25]. Three basic mechanisms for oxygen transportation are reported for oxide catalysts, (1) a surface redox mechanism – surface oxygens of the catalyst are transferred on to the surface of soot at the soot-

* Corresponding author.
E-mail address: steven.suib@uconn.edu (S.L. Suib).

http://dx.doi.org/10.1016/j.apcatb.2016.08.052
0926-3373/

catalyst interface, and once transferred, gas phase oxygen fills the resulting vacancies [13,21], (2) a spill-over mechanism – oxygen is first adsorbed on to the surface of the catalyst and undergoes some dissociation forming active oxygen species which are then subsequently transferred onto the surface of soot (catalyst-soot contact is not necessarily required) [21,26], (3) a redox mechanism – catalyst get reduced by transferring bulk oxygen to soot and gets oxidized [2,21].

Nanocrystalline mesoporous materials play a significant role in many applications such as catalysis, electronics, sorption, optics, gas sensors, and magnetics. Catalytic activities of nanocrystalline mesoporous materials are reported to be superior to the nonporous counterparts of the same material due to tunable porosity, surface oxygen vacancies, and large surface areas which promote lattice oxygen mobility [12,27,28–32]. In particular, mesoporous transition metal oxides of Mn, Fe, and Co are recognized for tunable oxidation states which are important in catalyzing redox reactions [31]. However, due to the synthetic limitations of sol-gel chemistry of transition metal oxides, the successful synthesis of different crystalline phases of mesoporous metal oxides is a tedious process. The circumstances are even more critical for manganese oxides, which can be present in the range of stable oxides with different oxidation states such as Mn_2O_3, Mn_3O_4, polymorphs of MnO_2 (α-,β-,γ-,δ-, ε-, and λ-), and cation-stabilized octahedral molecular sieves (OMS) [28,30]. In the year 2013, a new series of mesoporous materials [University of Connecticut (UCT) mesoporous materials] was discovered by our group [27]. As an extension of the reported sol-gel method, a series of different crystalline phases of mesoporous manganese oxides [Mn_2O_3, ε-MnO_2, and cation-stabilized octahedral molecular sieves ($K_{2-x}Mn_8O_{16}$)] using amorphous mesoporous manganese oxide as the precursor, was also successfully synthesized by our group [28,30]. In general, manganese oxides are well known candidates for numerous catalytic applications due to their unique redox properties, low cost, and environment compatibility [30,33,34]. The synthesized mesoporous manganese oxides have shown superior activity both in CO oxidation [28], and methane oxidation [30]. In this work, we report low temperature oxidation of diesel soot in the presence of NO_2 using the afore-mentioned mesoporous manganese oxides prepared by the UCT method.

2. Experimental section

2.1. Synthesis of mesoporous manganese oxides

Mesoporous amorphous manganese oxide (Meso-Mn-A) was synthesized (see supporting information for detailed experimental procedure) via an inverse micelle templating method previously reported by our group [27]. The synthesized sample is labeled as Meso-Mn-A (amorphous) and used as a precursor for the synthesis of other mesoporous manganese oxides with different crystal structures. Scheme S1 (Supporting information) summarizes the experimental conditions used. Meso-Mn_2O_3 was formed by heating Meso-Mn-A at 450 °C for 1 h. Meso-ε-MnO_2, was synthesized by mild acid treatment of Meso-Mn-A with aqueous sulfuric acid (0.5 M) followed by heating at 70 °C for 2 h. Finally, Meso-Mn-A was treated with KCl (0.5 M) and aqueous sulfuric acid (0.5 M), and heated at 70 °C for 2 h to obtain Meso-OMS-2.

2.2. Catalyst characterization

Low angle and wide-angle powder X-ray diffraction (PXRD) analyses were performed on a Rigaku Ultima IV diffractometer operating at a beam voltage of 40 kV and a beam current of 44 mA using Cu Kα as a radiation source (λ = 0.15406 nm). Low-angle diffraction patterns were collected over a 2θ range of 0.5–10° with a continuous scan rate of 0.5° min^{-1}, where the wide angle PXRD diffraction patterns were collected at 0.02° steps over a 2θ range of 10–70° with a continuous scan rate of 1.0° min^{-1}. N_2 sorption experiments were conducted on a Quantachrome Autosorb iQ_2 automated sorption system. All the samples were degassed at 150 °C for 6 h under vacuum prior to measurement. The surface areas were calculated using the Brunauer–Emmett–Teller (BET) method. The desorption branch of the isotherm was used to calculate pore sizes and pore volumes. High-resolution transmission electron microscopy (HR-TEM) analysis was carried out on a JEOL 2010 FasTEM microscope with an accelerating voltage of 200 kV. H_2-Temperature Programmed Reduction (H_2-TPR) measurements were performed on a TPR-MS setup which is equipped with a Thermolyne 79300 model temperature programmable tube furnace, Cirrus MKS PPT residual gas analyzer, and a quadrupole mass selective detector. Approximately 0.100 g of catalyst was packed into a quartz tube (i.d. 7 mm) supported with quartz wool and pretreated in a 500 standard cubic centimeters (sccm) Ar atmosphere at 120 °C for 1 h prior to H_2-TPR experiments. H_2 (5 vol.%) balanced by pure Ar was used as the reducing agent at a flow rate of 500 sccm. The measurements were carried out from RT to 700 °C at a heating rate of 10 °C/min. To determine the oxidation behavior of the catalysts under different atmospheres, TPO experiments were performed using the same set-up used for H_2-TPR experiments described above. A 0.100 g of soot catalyst mixture (1:5 wt ratio) was packed into a quartz tube (i.d. 7 mm) supported with quartz wool and pretreated in a 500 sccm Ar atmosphere at 120 °C for 1 h prior to TPO experiments. The measurements were carried out from RT to 700 °C at a heating rate of 10 °C/min under two different feed gas compositions; 10% O_2 balanced by Ar, and 10% O_2 + 1000 ppm NO_2 balanced by Ar. The flow rate of the feed gas was 500 sccm for all the TPO studies.

2.3. Catalyst activity evaluation

The catalytic activity of the synthesized catalysts for soot combustion was evaluated at atmospheric pressure from 100 to 500 °C in a fixed-bed reactor (i.d. 7 mm) using a model soot, Printex-U. The soot-catalyst mixture was prepared by smoothly grinding soot and catalyst (1:5 wt: wt) in an agate mortar for one minute. Then the above prepared soot-catalyst mixture was diluted with SiC to prevent formation of any local hot spots inside the reactor bed. A fixed bed of soot-catalyst-SiC mixture (0.100 g) supported by quartz wool was used for each activity test. Before each activity test, the catalyst was pre-treated under helium at 120 °C for 30 min and then cooled to 100 °C. After pre-treatment, feed gas (1:1 mixture of air and Ar) was set at 20 sccm, thus giving a weight hourly space velocity (WHSV) of 12 L h^{-1} g^{-1}. The first injection was done at 100 °C and then the temperature was increased in 50 °C increments until 500 °C. The equilibrium time at each temperature was about 15 min. The outlet gas was analyzed using a gas chromatograph (SRI 8610C) equipped with a thermal conductivity detector (TCD). The effect of having NO_2 in the feed gas on catalytic oxidation of soot was also studied separately by using air + 1000 ppm NO_2 balanced by Ar as the feed gas under the afore-mentioned experimental conditions. In both atmospheres, blank experiments were carried out in the absence of catalysts, to observe the effect of SiC. Three separate catalytic runs were carried out for each catalyst under both atmospheres. The conversion of soot, x (%), is defined as the percentage of carbon dioxide produced at each temperature and calculated according to E 1:

$$\boldsymbol{x}(\%) = \frac{[\boldsymbol{CO_2}]_{\max} - [\boldsymbol{CO_2}]_t}{[\boldsymbol{CO_2}]_{\max}} \times 100\% \quad \text{(E1)}$$

In this equation, $[CO_2]_{max}$ is the highest normalized peak area of CO_2 and $[CO_2]_t$ is the normalized peak area of CO_2 at a given

temperature. Activities of the catalysts were compared using characteristic temperatures such as soot ignition temperature (T_i), and the maximal conversion temperature (T_m), at which the soot conversions are 10% and 90%, respectively. Turnover Frequencies (TOF) were calculated according to E2 [30]:

$$TOF = \frac{\text{mol}_{\boldsymbol{carbon}} \times \text{h}^{-1}}{\text{mol}_{\boldsymbol{catalyst}}} \quad \text{(E2)}$$

Here, $\text{mol}_{\text{carbon}}$ is the number of moles of carbon converted per hour, and $\text{mol}_{\text{catalyst}}$ is the number of moles of catalyst.

2.4. Soot oxidation activation energy

The activation energy (E_a) was calculated according to the Ozawa method using the TGA/MS data according to Eq. (E3) [15,35,36]. The soot, catalyst, and SiC mixture (1:5:10 wt ratio) was measured over a temperature range of 200–700 °C with heating rates (B) of 2, 5, and 10 °C/min under similar feed gas compositions used for the catalytic studies. The value of the absolute temperature ($T\alpha$), at which a fixed fraction (~95%) α, of the soot is combusted for each heating rate, was obtained from the TG curve.

$$ln\ B = -0.4567\ \frac{E_a}{RT_\alpha} + C \quad \text{(E3)}$$

Here, C is a constant value with regards to the reaction.

3. Results

3.1. Catalyst characterization

3.1.1. Powder X-ray diffraction (PXRD)

In general, mesoporous manganese oxides synthesized via UCT method demonstrate a single low-angle PXRD diffraction line and a Type IV N_2 adsorption isotherm [27,28,30]. Fig. 1a (i–iv) shows low angle diffraction patterns of the catalysts. All the catalysts show a characteristic single low angle peak which confirms the regular mesostructure [27,28,30]. The position of the low angle diffraction line was found to be around ~12.5 nm for all the catalysts. The wide angle diffraction patterns are shown in Fig. 1b (i–iv), and all the patterns except for amorphous manganese oxide (Meso-Mn-A) could be well indexed with the JCPDS database confirming the absence of any other bulk crystalline phases. Meso-Mn_2O_3 (bixbyte, JCPDS 071 0646), Meso-ε-MnO_2 (akhtenskite, JCPDS 030 0820), and Meso-OMS-2 (cryptomelane, JCPDS 044 1386) were thus identified and confirmed the crystalline phases of the materials. Table 1 summarizes the structural parameters obtained for the synthesized matrials. Meso-Mn-A showed a low angle peak at 10.4 nm. Meso-Mn_2O_3 showed a low angle peak at 13.5 nm and the increase can be attributed to a unit cell expansion resulting from nanoparticle sintering occurred upon heat treatment [28], Meso-Mn-A did not show any diffraction lines whereas heat treatment of Meso-Mn-A yielded Meso-Mn_2O_3 having a crystallite size of 13.6 nm. Mild acid treatment of Meso Mn-A yielded Meso-ε-MnO_2 with a crystallite size of 2.1 nm. Meso-ε-MnO_2 is a rather less well known phase of MnO_2, however the structure is very similar to γ-MnO_2 [37]. The cryptomelane phase of MnO_2 (Meso-OMS-2) was obtained by a mild acid treatment of Meso-Mn-A in the presence of K^+. The crystallite size of the resultant Meso-OMS-2 was 4.1 nm.

3.1.2. N_2-Sorption studies

N_2 sorption isotherms and BJH desorption pore size distributions of mesoporous manganese oxides are shown in Fig. 2a and b, respectively. BET surface areas, pore sizes, and pore volumes are summarized in Table 1. All materials clearly display Type IV adsorption isotherms followed by Type I hysteresis loop which further confirm the regular mesostructure of the materials [28,30]. Acid-treated samples (Meso-ε-MnO_2 and Meso-OMS-2) show larger mesopore sizes than the precursor material Meso-Mn-A (3.4 nm). Meso- Mn_2O_3 and Meso-OMS-2 show moderate pore sizes of 4.9 nm and 6.6 nm respectively while Meso-ε-MnO_2 has the largest pore size of 7.8 nm. In addition, all mesoporous manganese oxides exhibit high surface area with Meso-Mn-A being the highest (165 m^2/g). The decreasing order of the surface area of the prepared catalysts were Meso-Mn-A (165 m^2/g) > Meso-OMS-2 (150 m^2/g) > Meso-ε-MnO_2 (94 m^2/g) > Meso-Mn_2O_3 (88 m^2/g). The order of the surface area is in excellent agreement with previously published data [28].

3.1.3. High-resolution transmission electron microscopy (HR-TEM)

The structure of the samples was examined using high-resolution transmission electron microscopy to evaluate the origin of mesoporosity of the materials. Direct heat treatment of Meso-Mn-A (Fig. S1a, Supporting information) results in Meso-Mn_2O_3 (Fig. S1b), but there is no prominent change in the smooth morphology shown by Meso-Mn-A. Both materials show aggregates of nanoparticles with interparticle voids. However, mild acid treatment has led to a significant difference in the structures of both Meso-ε-MnO_2 (Fig. S1c), and Meso-OMS-2 (Fig. S1d). In contrast to Meso-Mn-A and Meso-Mn_2O_3, the origin of mesoporosity was not clear for both Meso-ε-MnO_2 and Meso-OMS-2. However, flakes with wide openings grow out from the spherical particles which is very consistent with the literature [28,30]. The tunnel like octahedral molecular sieve (OMS) MnO_2 materials are known to show a variety of surface morphologies of fibers, needles, flakes, nanoplates etc. [37–39]. In accordance with the surface morphology reported for OMS-2, the synthesized Meso-OMS-2 (Fig. S1d) also showed the needle like nature further confirming the consistency of the material [28,30].

3.1.4. H_2-Temperature programmed reduction (H_2-TPR)

Manganese oxides are well known to catalyze a number of reactions due to their unique redox properties [38,40–42]. As most of heterogeneous catalytic reactions occur on the catalyst surface, high surface area, porosity, and readily interchangeable multiple oxidation states are found to be the most important features to have in a material to be active in oxidation reactions [28]. However, from a standpoint of a pure redox activity, the reducing ability of a species directly correlates with redox activity because their reduction generally occurs at a lower temperature [28,30]. Redox properties of the manganese oxides were investigated by H_2-TPR (Fig. S2).

Table 1
Structural parameters of mesoporous manganese oxide samples.

Sample ID	Low angle PXRD peak position (nm)	Surface area S_{BET} (m^2/g)	BJH des. pore size (nm)	BJH. ads. pore size (nm)	Pore volume (cc/g)	Scherer crystal size (nm)	Crystal structure
Meso-Mn-A	10.4	165	3.4	3.9	0.17	NA[a]	amorphous
Meso-Mn_2O_3	13.5	88	4.9	7.2	0.18	13.6	bixbyite
Meso-ε-MnO_2	15.5	94	7.8	10.7	0.26	2.1	akhtenskite
Meso-OMS-2	10.6	150	6.6	10.0	0.39	4.1	cryptomelane

[a] Not Applicable.

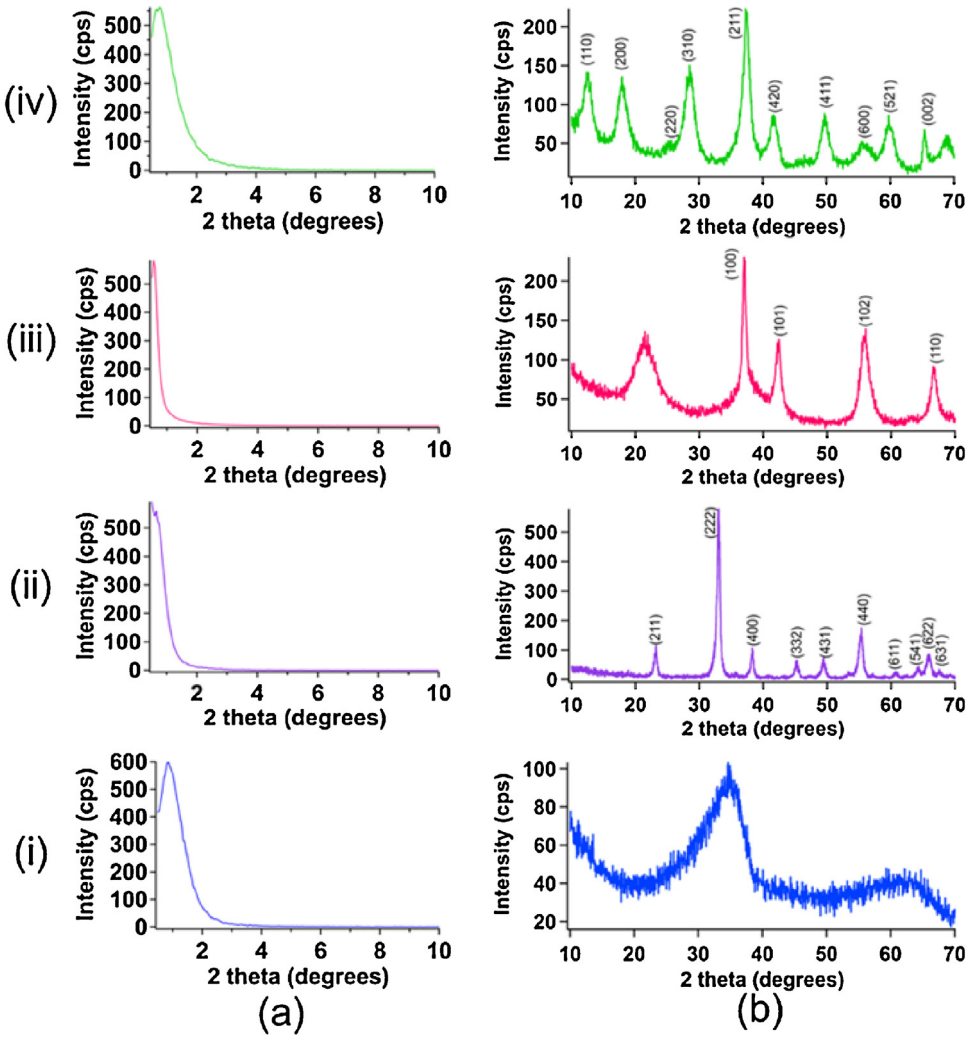

Fig. 1. Powder X-ray diffraction patterns of mesoporous manganese oxides: low-angle PXRD patterns (a), wide-angle PXRD patterns (b). [Meso-Mn-A (amorphous) (i), Meso-Mn_2O_3 (bixbyite) (ii), Meso-ε-MnO_2 (akhtenskite) (iii), and Meso-OMS-2 (cryptomelane) (iv)].

Meso-Mn-A showed the lowest reduction temperature at 313 °C, followed by a more prominent two-step reduction at 394 °C, and 473 °C. Meso-Mn_2O_3 showed the lowest reducing ability by having a two-step reduction at 414 °C, and 524 °C. The two step reduction of Meso-Mn_2O_3 could be attributed to the reduction of Mn_2O_3 to Mn_3O_4, followed by reduction of Mn_3O_4 to MnO [30,43]. Meso-ε-MnO_2 was reduced in two steps at 346 °C, and 486 °C with a ratio of 2 for the lower temperature peak to the higher temperature peak. This behavior can be assigned to first reduction of MnO_2 to Mn_3O_4 followed by reduction of Mn_3O_4 to MnO [28,30,43]. Finally, Meso-OMS-2 again showed a two step reduction at 345 °C, and 456 °C. The ratio of the two peaks are closer to 1 and therefore the two step reduction can be assigned to reduction of MnO_2 to Mn_2O_3 followed by reduction of Mn_2O_3 to MnO [28,30,43]. When mesoporous manganese oxides are compared based on their lowest temperature reduction peaks, the reducibility decreases in the order of Meso-Mn-A > Meso-ε-MnO_2 ≈ Meso-OMS-2 > Meso-Mn_2O_3.

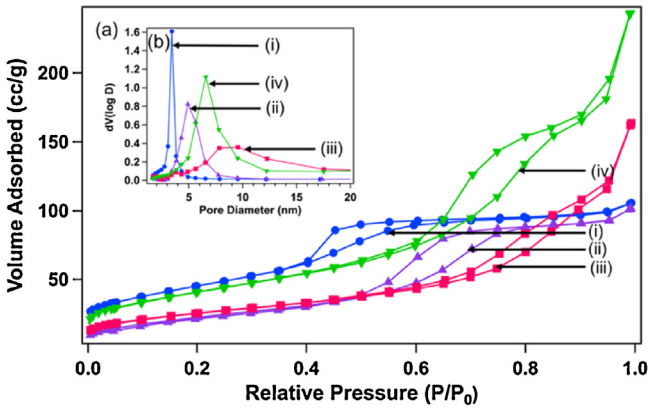

Fig. 2. N_2-sorption isotherms (a), and BJH desorption pore size distributions (b) of mesoporous manganese oxides. [Meso-Mn-A (i), Meso-Mn_2O_3 (ii), Meso-ε-MnO_2 (iii), and Meso-OMS-2 (iv)].

3.1.5. Temperature programmed oxidation (TPO)

In NO_2 assisted soot catalytic oxidation, the role of NO_2 is to "ignite" the soot at relatively low temperatures and at high temperatures O_2 dominates the oxidation [1]. Therefore, it is important to study the catalytic behavior of the mesoporous manganese oxides under both pure air and NO_2 + air atmospheres. The TPO experiments were carried out by feeding different feed gas compositions namely, 10% O_2 balanced by Ar, and 10% O_2 + 1000 ppm NO_2 balanced by Ar. Under both environments catalysts were 100% selective to CO_2 and no incomplete oxidation products are observed. Fig. 3a shows the TPO curves obtained during soot oxidation under 10% O_2 balanced by Ar. Meso-OMS-2 shows a miniature peak around 254 °C and is considered as CO_2 produced from resid-

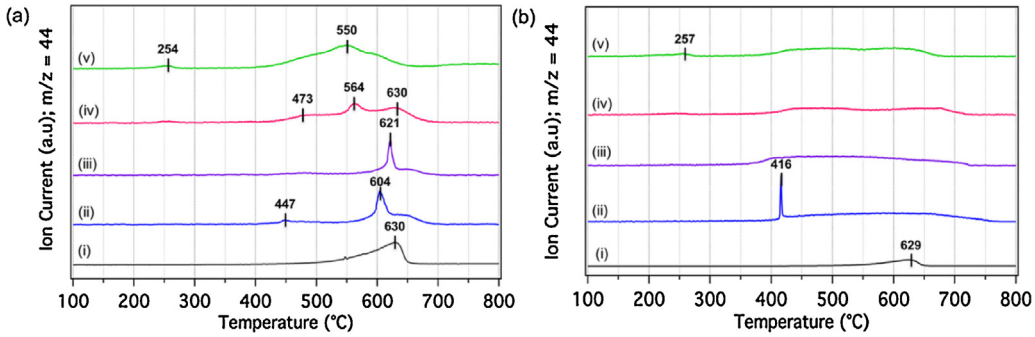

Fig. 3. TPO profiles of mesoporous manganese oxides: 10% O_2 balanced by Ar (a) and 1000 ppm NO_2 + 10% O_2 balanced by Ar (b). [Blank (i), Meso-Mn-A (ii), Meso-Mn_2O_3 (iii), Meso-ε-MnO_2 (iv), and Meso-OMS-2 (v)].

ual surfactant from the synthesis. However, none of the other catalysts showed a peak around this region and therefore that peak is excluded in further discussion. Meso-Mn-A showed the lowest onset oxidation temperature at 447 °C, followed by another peak at 604 °C. Meso-Mn_2O_3 showed a single oxidation peak around 621 °C. The oxidation of soot has occurred in three steps at 473 °C, 564 °C, and 630 °C by Meso-ε-MnO_2. Finally, Meso-OMS-2 showed a single broad peak distributed around 550 °C.

The soot oxidation behavior under 10% O_2 + 1000 ppm NO_2 balanced by Ar was expected to shift further left, towards much lower temperatures. However, under 10% O_2 balanced by Ar environment (Fig. 3b) only Meso-Mn-A showed a sharp onset temperature at 416 °C (relatively low onset temperature than under 10% O_2 balanced by Ar). The rest of the catalysts showed a broad temperature range for the oxidation. Meso-Mn_2O_3 shows a broad oxidation range from 380 °C to 715 °C. However, the onset temperature of oxidation was far below than that under pure O_2 environment which was about 600 °C. The oxidation temperature range for both Meso-ε-MnO_2 and Meso-OMS-2 in the presence of NO_2 are more or less similar to the oxidation temperature observed only with O_2. According to TPO results, Meso-Mn-A and Meso-Mn_2O_3 are more activated by the presence of NO_2 in the feed gas compared to Meso-ε-MnO_2 and Meso-OMS-2.

3.2. Catalyst activity evaluation

Catalytic soot oxidation activities of the mesoporous manganese oxides were evaluated by plotting conversion (%) vs. temperature profiles under two different feed gas compositions. Activities of the catalysts were compared using characteristic temperatures such as soot ignition temperature (T_i), and the maximal conversion temperature (T_m), temperatures at which the soot conversions are 10% and 90%, respectively and the results are summarized in Table 2. All the catalysts show 100% selectivity towards CO_2 under both environments. The selectivities to CO_2 in uncatalyzed reactions were above 80%. However, both CO and CO_2 were considered for calculating the percent conversion for the uncatalyzed reactions. Fig. 4a and b show the activity profiles of mesoporous manganese oxides under air balanced by Ar, and air + 1000 ppm NO_2 balanced by Ar, respectively. Mesoporous manganese oxides ignite soot at noticeably lower temperatures than the blank soot ignition temperature of 400 °C. In the absence of NO_2 there is a noticeable difference in ignition temperatures among the catalysts. The increasing order of ignition temperature is Meso-ε-MnO_2 (243 °C) < Meso-OMS-2 (278 °C) < Meso-Mn-A (329 °C) < Meso-Mn_2O_3 (349 °C) in air, whereas in the presence of NO_2, the ignition temperature is around 233 °C for all the materials. However, when T_m is set as the standard temperature to compare the activity, the increasing order of activity in air follows the order of Meso-Mn-A (442 °C) < Meso-Mn_2O_3 (436 °C) < Meso-OMS-2 (358 °C) < Meso-ε-MnO_2 (355 °C). In the presence of NO_2, T_m has decreased approximately by 100 °C for both Meso-Mn-A and Meso-Mn_2O_3, but the difference is only about 50 °C for Meso-ε-MnO_2 and Meso-OMS-2. However, Meso-ε-MnO_2 achieves the oxidation at the lowest temperature regardless of the composition of the feed gas. The increasing order of activity in the presence of NO_2 is, Meso-Mn-A (334 °C) < Meso-Mn_2O_3 (323 °C) < Meso-OMS-2 (316 °C) < Meso-ε-MnO_2 (305 °C).

3.3. Activation energy of soot oxidation

The activation energy (E_a) was calculated according to the Ozawa method [15,35,36], using the TGA-MS data. The soot and catalyst mixture (1:5 wt ratios) was measured over a temperature range of 200–700 °C with heating rates (B) of 2, 5, and 10 °C/min in air atmosphere. The value of the absolute temperature (Tα), at which a fixed fraction (~95%), α, of the soot is combusted for each heating rate was obtained from the TG curve. The soot oxidation kinetics inside a TGA furnace may slightly differ from a fixed-

Table 2
Ignition temperature (T_i), maximal conversion temperature (T_m), turnover frequency (TOF), and activation enrgy (E_a) of the catalysts for soot oxidation under different feed gas compositions.

Catalyst	Ar + Air				1000 ppm NO_2/Ar + Air			
	[a]T_i	[a]T_m	[b]TOF (h^{-1})	[f]E_a (kJ mol^{-1})	[a]T_i	[a]T_m	[b]TOF (h^{-1})	[f]E_a (kJ mol^{-1})
Meso-Mn-A	329	442	0.67	314	231	334	0.83	198
Meso-Mn_2O_3	349	436	0.67	318	235	323	0.83	317
Meso-ε-MnO_2	243	355	0.40	292	230	305	0.51	298
Meso-OMS-2	278	358	4.22	329	235	316	4.69	299
Blank	400	[c]451	*	401	406	493	*	399

[a] T_i and ^aT_m represent the temperatures at which soot conversions are 10 and 90%, respectively.
[b] TOF–[(mol $_{carbon}$)(mol $_{catalyst}$)$^{-1}$], where mol $_{carbon}$ is the moles of carbon soot converted per hour and mol $_{catalyst}$ is the moles of the catalyst.
[c] Maximal conversion was only 56% (Considering both CO and CO_2 in calculation).
[*] Did not calculate.
[f] Calculated using Ozawa method using TGA-MS data.

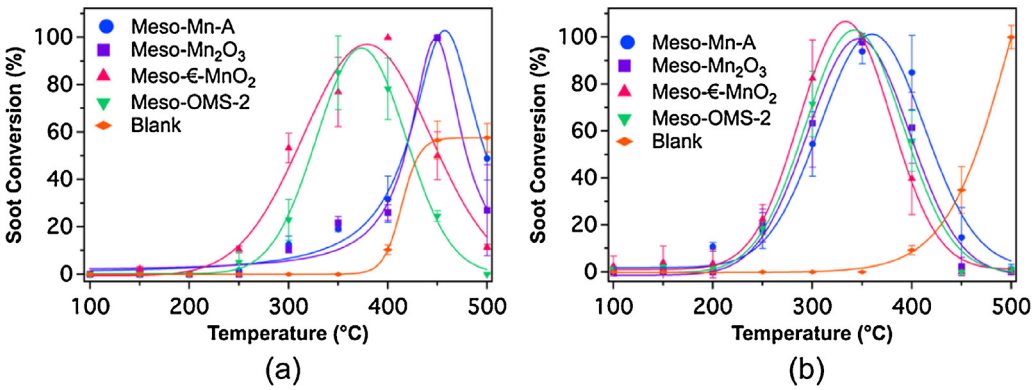

Fig. 4. Conversion (%) vs. temperature profiles of mesoporous manganese oxides: air balanced by Ar (a), and air + 1000 ppm NO_2 balanced by Ar (b).

bed reactor due to diffusion limitations [44]. However, it is still worth performing kinetic studies to interpret soot oxidation activity of the materials. TGA-MS profiles for all the materials under air balanced by argon are given in Fig. 5. According to the TGA-MS profile of Meso-Mn-A (Fig. 5a), there are two major weight loss regions at each heating rate, which implies that soot oxidation occurs in two steps for Meso-Mn-A. Meso- Mn_2O_3 shows a minor weight loss at about 400 °C, however the major oxidation occurs around 600 °C. Meso-ε-MnO_2 shows a single major weight loss around 400 °C confirming that all the soot gets oxidized in this region. Finally, Meso-OMS-2 also shows a single, relatively broader peak around 425 °C. The increasing order of activity according to TGA-MS data is Meso- Mn_2O_3 < Meso-Mn-A < Meso-OMS-2 < Meso-ε-MnO_2 which correlates with the order of activity obtained from the fixed bed reactor. The calculated activation energies are given in Table 2 and the relevant Ozawa kinetic plots are provided in Supplementary information (Figs. S3 and S4). Among all materials Meso-ε-MnO_2 has the lowest kinetic energy of ~295 kJ mol^{-1} under both feed gas compositions. Fig. 6 shows the TGA-MS profiles of all the materials under air + 1000 ppm NO_2 balanced by argon. Soot oxidation is catalyzed in a much broader range by Meso-Mn-A (Fig. 6a). The pattern of oxidation is significantly different for Meso-Mn-A compared to the two step oxidation in the absence of NO_2 in the feed gas. Although the oxidation temperature has shifted to the lower side, the behavior of soot oxidation has not drastically changed for both Meso-Mn_2O_3 and Meso-ε-MnO_2 (Fig. 6b and c). However, the temperature region for the oxidation has become much narrower for Meso-OMS-2 in the presence of NO_2 (Fig. 6d). The calculated activation energy for Meso-Mn-A has drastically dropped from 314 kJ mol^{-1} to 198 kJ mol^{-1} in the presence of NO_2, further supporting the considerable enhancement of activity of Meso-Mn-A. However, the calculated activation energies for Meso-Mn_2O_3 (~318 kJ mol^{-1}) and Meso-ε-MnO_2 (~295 kJ mol^{-1}) have not changed upon the composition of the feed gas. Finally, the calculated activation energy for Meso-OMS-2 has dropped down to 299 kJ mol^{-1} in the presence of NO_2 in the feed gas.

4. Discussion

In the present study, NO_2 assisted soot catalytic oxidation over mesoporous manganese oxides was investigated. In light of the soot oxidation activity results presented above, the mesoporous manganese oxides studied here offer several advantages. The first advantage is the 100% selectivity towards CO_2 regardless of the

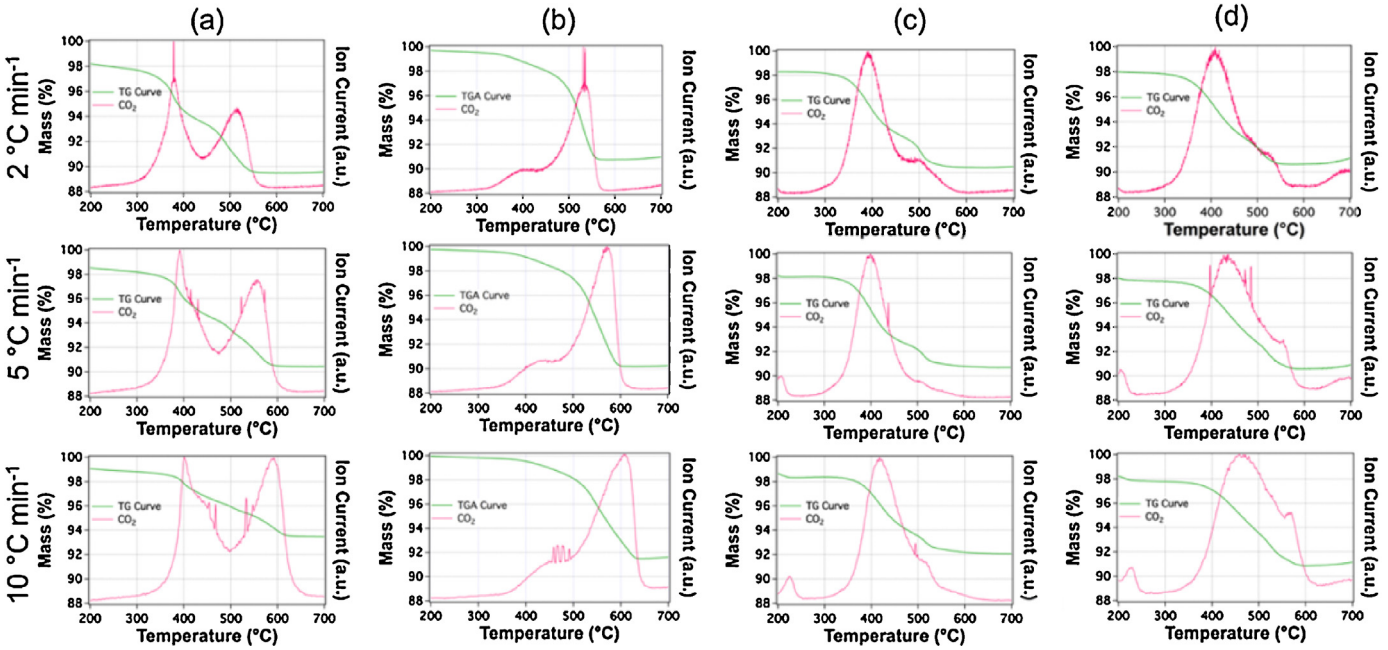

Fig. 5. TGA-MS profiles of soot oxidation on mesoporous manganese oxides under air balanced by argon at three different heating rates (2,5, and 10 °C/min). [Meso-Mn-A (a), Meso-Mn_2O_3 (b), Meso-ε-MnO_2 (c), and Meso-OMS-2 (d)].

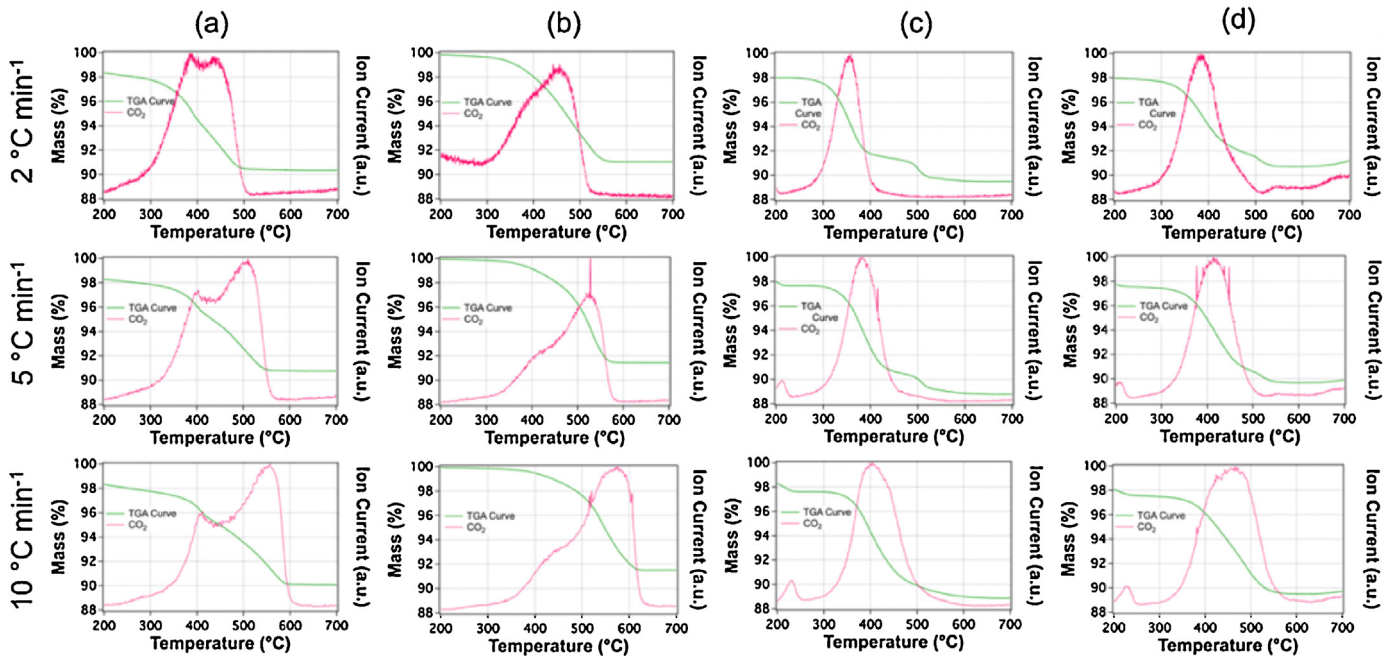

Fig. 6. TGA-MS profiles of soot oxidation on mesoporous manganese oxides under air + 1000 ppm NO_2 balanced by argon at three different heating rates (2, 5, and 10 °C/min). [Meso-Mn-A (a), Meso-Mn_2O_3 (b), Meso-ε-MnO_2 (c), and Meso-OMS-2 (d)].

atmosphere used. Even though the catalytic reactions were carried out under lean air conditions, with depleting the amount of oxygen present, it is possible to produce CO which is an issue for some reported materials [16]. The second advantage is being active in exhaust gas temperatures (200–500 °C), hence no additional energy is required for the functioning of the materials.

The reducibility of a catalyst is a very important factor which governs an oxidation reaction [28,30]. In general, the materials which reduce at lower temperatures are more active in redox activities [28]. Fig. 3 shows H_2-TPR profiles of manganese oxides. Meso-Mn-A showed the lowest reduction temperature at 314 °C, followed by a more prominent two-step reduction at 394 °C, and 473 °C. From a view of pure redox activity, Meso-Mn-A is expected to show the highest activity in soot oxidation. However, Meso-ε-MnO_2 is the second most reducible species and shows the best activity. The discrepancy may be due to the fact that although Meso-Mn-A shows the lowest reduction temperature, the peak area is very low suggesting a smaller amount of active sites. This is further confirmed by the TGA-MS profile of Meso-Mn-A (Fig. 5a) which shows a two step oxidation process. At lower temperature Meso-Mn-A initiates the oxidation and the total amount of soot cannot be oxidized due to the lack of active sites at that particular temperature. Meso-ε-MnO_2 was reduced in two steps at 346 °C, and 486 °C with a ratio of 2 for the lower temperature peak to the higher temperature peak. This behavior can be assigned to first reduction of MnO_2 to Mn_3O_4 followed by reduction of Mn_3O_4 to MnO [28,30,43].

Mesoporous manganese oxides ignite soot at noticeably low temperatures than the blank soot ignition temperature of 400 °C. When T_m is set as the standard temperature to compare the activity, the increasing order of activity in pure air atmosphere follows the order of Meso-Mn-A (438 °C) < Meso-Mn_2O_3 (436 °C) < Meso-OMS-2 (358 °C) < Meso-ε-MnO_2 (355 °C). In the presence of NO_2, T_m has decreased by approximately by 100 °C for both Meso-Mn-A and Meso-Mn_2O_3, but the decrease is only about 50 °C for Meso-ε-MnO_2 and Meso-OMS-2. However, under both feed gas compositions Meso-ε-MnO_2 achieves oxidation at the lowest temperature. Finally, the increasing order of activity in the presence of NO_2 is, Meso-Mn-A (334 °C) < Meso-Mn_2O_3 (323 °C) < Meso-OMS-2 (316 °C) < Meso-ε-MnO_2 (305 °C).

These results show that the increasing order of activity under either feed gas compositions does not correlate with the increasing order of surface area [Meso-Mn-A (165 m^2/g) > Meso-OMS-2 (150 m^2/g) > Meso-ε-MnO_2 (94 m^2/g) > Meso-Mn_2O_3 (88 m^2/g)] of the materials. Thus the assumption that soot oxidation occurs through a surface redox mechanism where soot-catalyst contact is necessary for the reaction to proceed is eliminated. NO_2 is a better oxidant than O_2, and therefore NO_2 ignites soot at relatively low temperatures and the oxidation is governed by O_2 at higher temperatures [1,3,45]. Literature reports suggest that NO_2-assisted soot oxidation occurs via formation of surface oxygen complexes (SOCs) followed by the decomposition of SOCs. The soot oxidation by NO_2 is a well explained in many literature reports [10,13,36,45]. The formation of SOCs may occur via many different pathways, however, the onset temperatures may vary depending on the oxidant [10]. In the absence of NO_2, oxygen is first adsorbed onto the surface of the catalyst and undergoes some dissociation forming active oxygen species (O*) which are then subsequently transferred onto the surface of soot to form SOCs (E4) via a possible spill-over mechanism [21,36]. The generated SOCs are known to be more reactive than bare soot and therefore the combustion of soot is greatly accelerated when there are SOCs on the surface [1]. Eqs. (E5) and (E6) represent the formation of SOCs in the presence of NO_2 [10,36,45–47]. The formation of SOCs may occur via direct interaction of free NO_2 present in the feed gas with soot (E5) or from the nitrates stored on manganese oxides (E6) at lower temperatures [10,45,48,49]. However, a delay of onset temperature in the absence of NO_2 was observed in both fixed bed catalytic studies as well as in TGA-MS experiments.

(4) $C_{soot} + O^* \rightarrow C(O)$

(5) $C_{soot} + NO_2 \rightarrow C(O) + NO$

(6) $C_{soot} + Mn^{x+} - NO_3 \rightarrow C(O) + Mn^{x+} - O + NO$

In general, oxidation reactions are catalyzed by manganese oxides are anticipated to occur through a Mars-van-Krevelen reaction mechanism [21,30,43,50,51]. Critical roles of structural defects

and the significance of mobility of lattice oxygen are highlighted through this mechanism. In here, the formed SOCs are oxidized at the soot-catalyst interface via reacting with lattice oxygen (E7 & E8). The interaction is facilitated by the diffusion of lattice oxygen from the bulk to its surface [49,50,52,53].

$$C(O) + 2O^{2-}(\text{lattice/surface}) + 4Mn^{4+} \rightarrow CO_2 + 4Mn^{3+} \quad (7)$$

$$C(O) + 2O^{2-}(\text{lattice/surface}) + 4Mn^{3+} \rightarrow CO_2 + 4Mn^{2+} \quad (8)$$

The catalytic performance of a certain catalyst is governed by the activation energy and the reaction pathway [36]. The calculated activation energy for Meso-Mn-A has drastically dropped from 314 kJ mol^{-1} to 198 kJ mol^{-1} in the presence of NO_2, further supporting a drastic enhancement of activity of Meso-Mn-A. Meso-Mn-A materials are more active in storing NO_2 as surface nitrate species which aid in generating SOCs according to E6. However, the calculated activation energies for Meso-Mn_2O_3 (~318 kJ mol^{-1}) and Meso-ε-MnO_2 (~295 kJ mol^{-1}) have not changed upon the composition of the feed gas. Finally, the calculated activation energy for Meso-OMS-2 has dropped down to 299 kJ mol^{-1} in the presence of NO_2 in the feed gas. Generally, the mechanism of soot oxidation reaction is mainly based on the reaction of soot with O_2, and NO_2 is considered as an intermediate which aids in reducing the activation energy of the reaction via igniting soot at lower temperatures to create SOCs [45].

5. Conclusion

Mesoporous UCT manganese oxides with crystal structures of amorphous, Mn_2O_3, ε-phase MnO_2, and cryptomelane type OMS-2 were shown to be excellent catalysts for NO_2 assisted soot oxidation in the present study. A strong synergetic effect of redox activity of manganese oxides and ability NO_2 in igniting soot at low temperature was observed. The experiments demonstrated that mesoporous MnO_2 (epsilon phase) (Meso-ε-MnO_2) has the highest catalytic activity for soot oxidation in the presence of NO_2 in the feed gas (T_{90} = 305 °C), the narrowest temperature range (75 °C), and the lowest E_a (298 kJ mol^{-1}). Regardless of the superior performance of Meso-ε-MnO_2, the soot oxidation activities of Meso-Mn-A and Meso-Mn_2O_3 are greatly enhanced in the presence of NO_2, compared to its effect on Meso-ε-MnO_2. In conclusion, NO_2 is considered as an intermediate which aids in reducing the activation energy of the reaction via igniting soot at lower temperatures to create SOCs for Meso-ε-MnO_2.

Author information

Notes.
The authors declare no competing financial interest.

Acknowledgements

The authors are grateful for support of the U.S Department of Energy, Office of Basic Energy Sciences, Division of Chemical, Biological and Geochemical Sciences under Grant DE_FGO2-86ER13622.A000.

Appendix A. Supplementary data

Supplementary data associated with this article can be found, in the online version, at http://dx.doi.org/10.1016/j.apcatb.2016.08.052.

References

[1] S. Liu, X. Wu, D. Weng, M. Li, R. Ran, Roles of acid sites on Pt/H-ZSM5 catalyst in catalytic oxidation of diesel soot, ACS Catal. 5 (2015) 909–919, http://dx.doi.org/10.1021/cs5018369.
[2] S. Wagloehner, M. Nitzer-Noski, S. Kureti, Oxidation of soot on manganese oxide catalysts, Chem. Eng. J. 259 (2015) 492–504, http://dx.doi.org/10.1016/j.cej.2014.08.021.
[3] K. Tikhomirov, O. Kröcher, M. Elsener, A. Wokaun, MnOx-CeO2 mixed oxides for the low-temperature oxidation of diesel soot, Appl. Catal. B Environ. 64 (2006) 72–78, http://dx.doi.org/10.1016/j.apcatb.2005.11.003.
[4] M.V. Twigg, P.R. Phillips, Cleaning the air we breathe—controlling diesel particulate emissions from passenger cars, Platin. Met. Rev. 53 (2009) 27–34, http://dx.doi.org/10.1595/147106709X390977.
[5] L. Castoldi, E. Aneggi, R. Matarrese, R. Bonzi, J. Llorca, A. Trovarelli, L. Lietti, Silver-based catalytic materials for the simultaneous removal of soot and NOx, Catal. Today 258 (2015) 405–415, http://dx.doi.org/10.1016/j.cattod.2015.02.024.
[6] H.N. Sharma, L. Pahalagedara, A. Joshi, S.L. Suib, A.B. Mhadeshwar, Experimental study of carbon black and diesel engine soot oxidation kinetics using thermogravimetric analysis, Energy Fuels 26 (2012) 5613–5625, http://dx.doi.org/10.1021/ef3009025.
[7] F. Qi, S. Xiong, Y. Liao, H. Dang, S. Yang, A novel dual layer SCR catalyst with a broad temperature window for the control of NOx emission from diesel bus, Catal. Commun. 65 (2015) 108–112, http://dx.doi.org/10.1016/j.catcom.2015.03.002.
[8] D. Gardini, J.M. Christensen, C.D. Damsgaard, A.D. Jensen, J.B. Wagner, Visualizing the mobility of silver during catalytic soot oxidation, Appl. Catal. B Environ. 183 (2016) 28–36, http://dx.doi.org/10.1016/j.apcatb.2015.10.029.
[9] S. Liu, X. Wu, Y. Lin, M. Li, D. Weng, Active oxygen-assisted NO-NO2 recycling and decomposition of surface oxygenated species on diesel soot with Pt/Ce0.6Zr0.4O2 catalyst, Chin. J. Catal. 35 (2014) 407–415, http://dx.doi.org/10.1016/S1872-2067(14)60004-8.
[10] X. Wu, F. Lin, H. Xu, D. Weng, Effects of adsorbed and gaseous NOx species on catalytic oxidation of diesel soot with MnOx-CeO2 mixed oxides, Appl. Catal. B Environ. 96 (2010) 101–109, http://dx.doi.org/10.1016/j.apcatb.2010.02.006.
[11] N. Guillén-Hurtado, A. García-García, A. Bueno-López, Active oxygen by Ce–Pr mixed oxide nanoparticles outperform diesel soot combustion Pt catalysts, Appl. Catal. B Environ. 174–175 (2015) 60–66, http://dx.doi.org/10.1016/j.apcatb.2015.02.036.
[12] L. Pahalagedara, H. Sharma, C.H. Kuo, S. Dharmarathna, A. Joshi, S.L. Suib, A.B. Mhadeshwar, Structure and oxidation activity correlations for carbon blacks and diesel soot, Energy Fuels 26 (2012) 6757–6764, http://dx.doi.org/10.1021/ef301331b.
[13] P. Sudarsanam, B. Hillary, B. Mallesham, B.G. Rao, M.H. Amin, A. Nafady, A.M. Alsalme, B.M. Reddy, S.K. Bhargava, Designing CuOx nanoparticle-decorated CeO2 nanocubes for catalytic soot oxidation: role of the nanointerface in the catalytic performance of heterostructured nanomaterials, Langmuir 32 (2016) 2208–2215, http://dx.doi.org/10.1021/acs.langmuir.5b04590.
[14] Y. Wei, Z. Zhao, X. Yu, B. Jin, J. Liu, C. Xu, A. Duan, G. Jiang, S. Ma, One-pot synthesis of core–shell Au@CeO2-δ nanoparticles supported on three-dimensionally ordered macroporous ZrO2 with enhanced catalytic activity and stability for soot combustion, Catal. Sci. Technol. 3 (2013) 2958, http://dx.doi.org/10.1039/c3cy00248a.
[15] C. Lee, J.-I. Park, Y.-G. Shul, H. Einaga, Y. Teraoka, Ag supported on electrospun macro-structure CeO2 fibrous mats for diesel soot oxidation, Appl. Catal. B Environ. 174–175 (2015) 185–192, http://dx.doi.org/10.1016/j.apcatb.2015.03.008.
[16] D. Uner, M.K. Demirkol, B. Dernaika, A novel catalyst for diesel soot oxidation, Appl. Catal. B Environ. 61 (2005) 334–345, http://dx.doi.org/10.1016/j.apcatb.2005.05.011.
[17] M. Zawadzki, W. Staszak, F.E. López-Suárez, M.J. Illán-Gómez, A. Bueno-López, Preparation, characterisation and catalytic performance for soot oxidation of copper-containing $ZnAl_2O_4$ spinels, Appl. Catal. A Gen. 371 (2009) 92–98, http://dx.doi.org/10.1016/j.apcata.2009.09.035.
[18] W.F. Shangguan, Y. Teraoka, S. Kagawa, W.F. Shangguan Er, Simultaneous catalytic removal of NO, and diesel soot particulates over ternary AB,O, spinel-type oxides, Appl. Catal. B Environ. Catal. B 8 (1996) 217–227, http://dx.doi.org/10.1016/0926-3373(95)00070-4.
[19] I. Atribak, I. Such-Basáñez, A. Bueno-López, A. García, Comparison of the catalytic activity of MO2 (M = Ti, Zr, Ce) for soot oxidation under NOx/O2, J. Catal. 250 (2007) 75–84, http://dx.doi.org/10.1016/j.jcat.2007.05.015.
[20] P. Miceli, S. Bensaid, N. Russo, D. Fino, CeO2-based catalysts with engineered morphologies for soot oxidation to enhance soot-catalyst contact, Nanoscale Res. Lett. 9 (2014) 254, http://dx.doi.org/10.1186/1556-276X-9-254.
[21] G. Mul, F. Kapteijn, C. Doornkamp, J.a. Moulijn, Transition metal oxide catalyzed carbon black oxidation: a study with $18O_2$, J. Catal. 179 (1998) 258–266.
[22] K. Tikhomirov, O. Kröcher, M. Elsener, A. Wokaun, MnOx-CeO2 mixed oxides for the low-temperature oxidation of diesel soot, Appl. Catal. B Environ. 64 (2006) 72–78, http://dx.doi.org/10.1016/j.apcatb.2005.11.003.
[23] X. Wu, Q. Liang, D. Weng, Z. Lu, The catalytic activity of CuO–CeO2 mixed oxides for diesel soot oxidation with a NO/O2 mixture, Catal. Commun. 8 (2007) 2110–2114, http://dx.doi.org/10.1016/j.catcom.2007.04.023.

[24] P.G. Harrison, I.K. Ball, W. Daniell, P. Lukinskas, M. Céspedes, E.E. Miró, M.a. Ulla, Cobalt catalysts for the oxidation of diesel soot particulate, Chem. Eng. J. 95 (2003) 47–55, http://dx.doi.org/10.1016/S1385-8947(03)00077-9.
[25] S. Liu, X. Wu, W. Liu, W. Chen, R. Ran, M. Li, D. Weng, Soot oxidation over CeO2 and Ag/CeO2: factors determining the catalyst activity and stability during reaction, J. Catal. 337 (2016) 188–198, http://dx.doi.org/10.1016/j.jcat.2016.01.019.
[26] N. Guillén-Hurtado, A. García-García, A. Bueno-López, Isotopic study of ceria-catalyzed soot oxidation in the presence of NOx, J. Catal. 299 (2013) 181–187, http://dx.doi.org/10.1016/j.jcat.2012.11.026.
[27] A.S. Poyraz, C.-H. Kuo, S. Biswas, C.K. King'ondu, S.L. Suib, A general approach to crystalline and monomodal pore size mesoporous materials, Nat. Commun. 4 (2013) 2952, http://dx.doi.org/10.1038/ncomms3952.
[28] A.S. Poyraz, W. Song, D. Kriz, C. Kuo, M.S. Seraji, S.L. Suib, Crystalline mesoporous K2-x Mn_8O_{16} and ε-MnO_2 by mild transformations of amorphous mesoporous manganese oxides and their enhanced redox properties, ACS Appl. Mater. Interfaces 20 (2014) 10986–10991.
[29] A.S. Poyraz, C. Kuo, E. Kim, Y. Meng, M.S. Seraji, S.L. Suib, Tungsten-promoted mesoporous group 4 (Ti, Zr, and Hf) transition- metal oxides for room-temperature solvent-free acetalization and ketalization reactions, Chem. Mater. 26 (2014) 2803–2813.
[30] N.D. Wasalathanthri, A.S. Poyraz, S. Biswas, Y. Meng, C.-H. Kuo, D.A. Kriz, S.L. Suib, High-performance catalytic CH4 oxidation at low temperatures: inverse micelle synthesis of amorphous mesoporous manganese oxides and mild transformation to K2-x Mn_8O_{16} and ε-MnO_2, J. Phys. Chem. C 119 (2015) 1473–1482, http://dx.doi.org/10.1021/jp5108558.
[31] W. Song, A.S. Poyraz, Y. Meng, Z. Ren, S. Chen, S.L. Suib, Mesoporous Co3O4 with controlled porosity: inverse micelle synthesis and high-performance catalytic CO oxidation at −60 °C, Chem. Mater. 26 (2014) 4639.
[32] S. Biswas, B. Dutta, K. Mullick, C.H. Kuo, A.S. Poyraz, S.L. Suib, Aerobic oxidation of amines to imines by cesium-promoted mesoporous manganese oxide, ACS Catal. 5 (2015) 4394–4403, http://dx.doi.org/10.1021/acscatal.5b00325.
[33] H. Chen, J. He, C. Zhang, H. He, Self-assembly of novel mesoporous manganese oxide nanostructures and their application in oxidative decomposition of formaldehyde, J. Phys. Chem. C 111 (2007) 18033–18038, http://dx.doi.org/10.1021/jp076113n.
[34] Z. Yang, Y. Zhang, W. Zhang, X. Wang, Y. Qian, X. Wen, S. Yang, Nanorods of manganese oxides: synthesis, characterization and catalytic application, J. Solid State Chem. 179 (2006) 679–684, http://dx.doi.org/10.1016/j.jssc.2005.11.028.
[35] N. Koga, Ozawa's kinetic method for analyzing thermoanalytical curves: history and theoretical fundamentals, J. Therm. Anal. Calorim. 113 (2013) 1527–1541, http://dx.doi.org/10.1007/s10973-012-2882-5.
[36] X. Guo, M. Meng, F. Dai, Q. Li, Z. Zhang, Z. Jiang, S. Zhang, Y. Huang, NOx-assisted soot combustion over dually substituted perovskite catalysts La1-xKxCo1-yPdyO3-δ, Appl. Catal. B Environ. 142–143 (2013) 278–289, http://dx.doi.org/10.1016/j.apcatb.2013.05.036.
[37] Y.-S. Ding, X.-F. Shen, S. Gomez, H. Luo, M. Aindow, S.L. Suib, Hydrothermal growth of manganese dioxide into three-dimensional hierarchical nanoarchitectures, Adv. Funct. Mater. 16 (2006) 549–555, http://dx.doi.org/10.1002/adfm.200500436.
[38] S. Liang, F. Teng, G. Bulgan, R. Zong, Y. Zhu, Effect of phase structure of MnO2 nanorod catalyst on the activity for CO oxidation, J. Phys. Chem. C (2008) 5307–5315.
[39] H. Huang, S. Sithambaram, C.-H. Chen, C. King'ondu Kithongo, L. Xu, A. Iyer, H.F. Garces, S.L. Suib, Microwave-assisted hydrothermal synthesis of cryptomelane-type octahedral molecular sieves (OMS-2) and their catalytic studies, Chem. Mater. 22 (2010) 3664–3669, http://dx.doi.org/10.1021/cm100220g.
[40] Y. Ding, X. Shen, S. Sithambaram, S. Gomez, R. Kumar, V.M.B. Crisostomo, S.L. Suib, M. Aindow, Synthesis and catalytic activity of cryptomelane-type manganese dioxide nanomaterials produced by a novel solvent-free method, Chem. Mater. 17 (2005) 5382–5389, http://dx.doi.org/10.1021/cm051294w.
[41] V. Makwana, The role of lattice oxygen in selective benzyl alcohol oxidation using OMS-2 catalyst: a kinetic and isotope-labeling study, J. Catal. 210 (2002) 46–52, http://dx.doi.org/10.1006/jcat.2002.3680.
[42] A.M. El-sawy, P.K. Dutta, S.L. Suib, Water oxidation catalysis using amorphous manganese oxides, octahedral molecular sieves (OMS-2), and octahedral layered (OL-1) manganese oxide structures, J. Phys. Chem. 116 (2012) 6474–6483.
[43] E.R. Stobbe, B.a. de Boer, J.W. Geus, The reduction and oxidation behaviour of manganese oxides, Catal. Today 47 (1999) 161–167, http://dx.doi.org/10.1016/S0920-5861(98)00296-X.
[44] I.C. Jaramillo, C.K. Gaddam, R.L. Vander Wal, J.S. Lighty, Effect of nanostructure, oxidative pressure and extent of oxidation on model carbon reactivity, Combust. Flame 162 (2015) 1848–1856, http://dx.doi.org/10.1016/j.combustflame.2014.12.006.
[45] Y. Wang, Y. Li, Preparation and NOx-assisted soot oxidation activity of a CuO–CeO2 mixed oxide catalyst, Chem. Eng. Sci. 2–3 (2015), http://dx.doi.org/10.1016/j.ces.2015.03.024.
[46] R. Matarrese, E. Aneggi, L. Castoldi, J. Llorca, A. Trovarelli, L. Lietti, Simultaneous removal of soot and NOx over K- and Ba-doped ruthenium supported catalysts, Catal. Today 267 (2016) 119–129, http://dx.doi.org/10.1016/j.cattod.2015.12.016.
[47] M.M. Azis, H. Härelind, D. Creaser, On the role of h2 to modify surface NOx species over Ag Al2O3 as Lean NOx reduction catalyst TPD and DRIFTS studies, Catal. Sci. Technol. 5 (2015) 296–309, http://dx.doi.org/10.1039/C4CY00816B.
[48] A. Setiabudi, J. Chen, G. Mul, M. Makkee, J. a. Moulijn, CeO2 catalysed soot oxidation: the role of active oxygen to accelerate the oxidation conversion, Appl. Catal. B Environ. 51 (2004) 9–19, http://dx.doi.org/10.1016/j.apcatb.2004.01.005.
[49] H. Ranji-Burachaloo, S. Masoomi-Godarzi, A.A. Khodadadi, Y. Mortazavi, Synergetic effects of plasma and metal oxide catalysts on diesel soot oxidation, Appl. Catal. B Environ. 182 (2016) 74–84, http://dx.doi.org/10.1016/j.apcatb.2015.09.019.
[50] V. Makwana, The role of lattice oxygen in selective benzyl alcohol oxidation using OMS-2 catalyst: a kinetic and isotope-labeling study, J. Catal. 210 (2002) 46–52, http://dx.doi.org/10.1006/jcat.2002.3680.
[51] S. Yin, Z. Wang, E.R. Bernstein, O-Atom transport catalysis by neutral manganese oxide clusters in the gas phase: reactions with CO, C2H4, NO2, and O2, J. Chem. Phys. 139 (2013), http://dx.doi.org/10.1063/1.4819059.
[52] Q. Liang, X. Wu, D. Weng, H. Xu, Oxygen activation on Cu/Mn–Ce mixed oxides and the role in diesel soot oxidation, Catal. Today 139 (2008) 113–118, http://dx.doi.org/10.1016/j.cattod.2008.08.013.
[53] B. Dutta, S. Biswas, V. Sharma, N.O. Savage, S.P. Alpay, S.L. Suib, Mesoporous manganese oxide catalyzed aerobic oxidative coupling of anilines to aromatic azo compounds, Angew. Chem. Int. Ed. 128 (2016) 2211–2215, http://dx.doi.org/10.1002/anie.201508223.